Linking snow microstructure to its macroscopic elastic stiffness tensor: A numerical homogenization method and its application to 3-D images from X-ray tomography

Antoine Wautier, Christian Geindreau, Frédéric Flin

Linking snow microstructure to its macroscopic elastic properties: a numerical homogenization method and its application to 3D images from X-ray tomography

A. Wautier,[1,2,3] C. Geindreau,[2,3] F. Flin,[1]

antoine.wautier@gmail.com, christian.geindreau@3sr-grenoble.fr, frederic.flin@meteo.fr

[1]Météo-France – CNRS, CNRM-GAME

UMR 3589, CEN, F-38400 Saint Martin

d'Hères, France

[2]Université Grenoble Alpes, 3SR, F-38000

Grenoble, France

[3]CNRS, 3SR, F-38000 Grenoble, France

We propose a modeling of the homogeneous behavior of snow based on the combined use of microtomography imaging and the resolution of Kinematically Uniform Boundary Condition (KUBC) problems derived from the homogenization theories. Snow is modeled as a porous cohesive material, and its 3D macroscopic mechanical behavior is explored within the framework of the elastic behavior of ice. Based on the integral range theory, a convergence analysis is performed in terms of physical and not geometrical parameters. This provides an accurate definition of the representative elementary volume to be used in numerical simulations.

A wide range of snow densities is explored (100 600 kg/m3) and a simple power law is proposed in order to link the Young and shear moduli of snow to its density. Thanks to the study of three temporal series, the influence of three types of metamorphism (a temperature gradient, a wet snow and an isothermal metamorphism) on the macroscopic elastic properties of snow is recovered in details through numerical simulations for one of the first times.

Keywords: homogenization, KUBC, elasticity, microtomography, finite elements, snow.

1. Introduction

Snow is a highly porous material that exists close to its melting point and exhibits a complex microstructure constantly evolving in time. Because overall mechanical properties of snow are strongly influenced by its density [*Mellor*, 1974] and the topology of its microstructure [*Shapiro et al.*, 1997], a correct multi-scale modeling of the mechanical properties of snow is of great interest when it comes to avalanche risk forecasting.

Recently, the generalization of X-ray tomography and its application to snow [*Brzoska et al.*, 1999; *Schneebeli*, 2004; *Kaempfer et al.*, 2005; *Flin and Brzoska*, 2008; *Srivastava et al.*, 2010; *Pinzer et al.*, 2012] enabled the description of its complex geometry down to the micro-scale. Nowadays, good databases of 3D images for the different snow types described in the international classification [*Fierz et al.*, 2009] are available [*Calonne et al.*, 2012; *Löwe et al.*, 2013].

With precise description of the ice skeleton of snow, its complex behavior can be investigated thanks to the fairly well established physical and mechanical properties of ice [*Schulson et al.*, 2009]. From this point, the macroscopic behavior of snow considered as a homogeneous material can be up-scaled thanks to the use of techniques derived from the homogenization theory based on the assumption of the separation of scales [*Dormieux and Bourgeois*, 2002; *Auriault et al.*, 2010]. In recent works, the combination of X-ray tomography imaging, finite elements techniques and ever increasing computing power was used to bridge the gap between the topology of the ice skeleton of snow and its mechanical behavior [*Schneebeli*, 2004; *Pieritz et al.*, 2004; *Srivastava et al.*, 2010; *Hagenmuller et al.*, 2014; *Chandel et al.*, 2014; *Schleef et al.*, 2014]. However while *Srivastava et al.*

[2010] used an approach rigorously based on the homogenization theory [*Van Rietbergen et al.*, 1996], most of the up-scaled snow properties found in the literature were obtained thanks to numerical simulations of "real" experiments assuming an isotropic macroscopic behavior [*Hagenmuller et al.*, 2014; **?**]. Moreover, while snow microstructure is generally anisotropic [*Calonne et al.*, 2012, 2014], most of the constitutive equations for snow mechanical behavior given in the literature are only unidimensional [*Mellor*, 1974].

In the wake of the study performed by *Calonne et al.* [2011, 2012, 2014] on the homogenization of the transfer properties of snow, the aim of this paper is to propose a rigorous multi-scale modeling of the elastic mechanical behavior of snow and to reckon the relative influence of the density and the topology of the microstructure on its macroscopic properties. Quantitative results are given for a very wide range of densities (from 100 to 600 kg/m^3) and the influence of different types of metamorphism is estimated.

In order to do so, boundary value problems derived from the homogenization theories were solved numerically on 3D snow images obtained by micro-tomography. Depending on the choice of the boundary value problem, the sample's representative elementary volume (REV) required to deduce the macroscopic mechanical properties varies. Three boundary value problems described in the homogenization theories are considered to give relatively small REV. From the biggest to the smallest ones [*Kanit et al.*, 2003], these three approaches are named SUBC (statically uniform boundary conditions), KUBC (kinematically uniform boundary conditions) and PBC (periodic boundary conditions). In the KUBC approach, a macroscopic homogeneous strain is imposed on the boundary. Conversely, in the SUBC approach a macroscopic homogeneous stress is imposed on the

boundary. In the PBC approach, mix stress/strain boundary conditions are applied by enforcing the periodicity of the displacement field over the three directions of space and the periodicity of the normal stress across the sample boundaries. If the PBC approach is supposed to be the best approach in terms of convergence with respect to the size of the REV [*Kanit et al.*, 2003], its application on a non-periodic porous microstructure is not straightforward. This requires for instance to wrap the sample into a virtual bounding box or to fill up the porosity with a soft material. In order to avoid the introduction of artifacts, the KUBC approach was retained.

2. KUBC numerical homogenization procedure

The whole numerical homogenization procedure can be decomposed into four steps that are summarized in Figure 1 and detailed in the following subsections.

2.1. Converting images into 3D meshes (step 1)

Thanks to the use of the Matlab open-source toolbox *iso2mesh* [*Fang and Boas*, 2009], a tetrahedral mesh was fitted onto the original 3D binary images of typical size 600^3 voxels. The toolbox was used with the *cgalmesh* utility option and adaptative meshes of controlled density and quality were created from binary snow images. The resulting meshes were composed of a typical number of 2 millions of elements and can be visualized in Figure 1.

2.2. Boundary value problem definition in Abaqus (step 2)

Under the assumption of the separation of scales, it is possible to deduce macro-properties of a given material by performing numerical tests on a representative elemen-

tary volume (REV), i.e. a volume that is "big enough" with respect to the size of the micro-structure to be considered as representative of the whole material and the physical phenomena. Then, thanks to Hill's lemma, the macroscopic stress tensor $\underline{\underline{\Sigma}}$ and strain tensor $\underline{\underline{\mathrm{E}}}$ are deduced from their microscopic counterparts ($\underline{\underline{\sigma}}$ and $\underline{\underline{\varepsilon}}$) by computing their mean values over the REV (V).

$$\underline{\underline{\mathrm{E}}} = \langle \underline{\underline{\varepsilon}} \rangle = \frac{1}{|V|} \int_V \underline{\underline{\varepsilon}} \, \mathrm{d}V, \qquad \underline{\underline{\Sigma}} = \langle \underline{\underline{\sigma}} \rangle = \frac{1}{|V|} \int_V \underline{\underline{\sigma}} \, \mathrm{d}V$$

Because of Green's formula, the mean stress and strain can either be averaged on the sample's volume or on its boundary. For instance, if $\underline{\underline{\varepsilon}}$ is kinematically admissible to a continuous displacement field $\underline{u}(\underline{x})$, the equivalent strain can be computed with the equivalent formula:

$$\underline{\underline{\mathrm{E}}} = \frac{1}{|V|} \int_{\partial V} \underline{u} \otimes_s \underline{n} \, \mathrm{d}S$$

where $\otimes_s$ is the symetrized tensorial product and $\underline{n}$ the outward normal vector on the boundary ∂V. With this localization property, a savvy choice in the boundary conditions enables the control of the macro stress or strain that is imposed on a given sample. And indirectly, this choice in the boundary conditions governs the size of the REV. In the present work, the KUBC approach was retained and practically implemented thanks to the use of the Abaqus plugin *HomTools* developed by *Lejeunes et al.* [2011]. The plugin enables the automatic definition of the linear relationship on ∂V between the displacements $\underline{u}$ and the macroscopic homogeneous strain $\underline{\underline{\mathrm{E}}}$ defined as $\underline{u} = \underline{\underline{\mathrm{E}}} \cdot \underline{x}$ for $\underline{x} \in \partial V$ (Figure 1).

2.3. Ice constitutive equation (step 3)

From a microscopic point of view, the ice skeleton is constituted of an assemblage of mono-crystalline particles. While some recent studies [*Riche et al.*, 2013] show that ice grain orientation in snow may be anisotropic under specific circumstances, in the following the poly-crystalline ice skeleton is considered as an homogeneous isotropic elastic material. Thus, the ice stiffness tensor $\underline{\underline{\underline{\underline{C}}}}^{\text{ice}}$ is defined as :

$$\underline{\underline{\sigma}} = \underline{\underline{\underline{\underline{C}}}}^{\text{ice}} : \underline{\underline{\varepsilon}} = \frac{E}{1+\nu}\left(\underline{\underline{\varepsilon}} + \frac{\nu}{1-2\nu}\text{Tr}(\underline{\underline{\varepsilon}})\underline{\underline{1}}\right),$$

where E and ν are the Young modulus and the Poisson ratio respectively, and $\underline{\underline{1}}$ is the second order identity tensor. The ice elastic properties presented in *Schulson et al.* [2009]; *Chandel et al.* [2014] show that E ranges from 0.2 GPa to 9.5 GPa. In order to leave aside the resulting huge uncertainties, all the results in this paper are presented in a dimensionless form by setting E equal to one. Based on the literature, the Poison's ratio ν is chosen equal to 0.3.

2.4. Computing the homogenized stiffness tensor (step 4)

The homogenization problem to be solved on the REV (V) is written:

$$\begin{cases} \underline{\text{div}}\,\underline{\underline{\sigma}} = 0 & \text{for } \underline{x} \in V \\ \underline{u} = \underline{\underline{\text{E}}} \cdot \underline{x} & \text{for } \underline{x} \in \partial V \\ \underline{\underline{\varepsilon}} = \frac{1}{2}\left(\underline{\underline{\nabla}}\,\underline{u} + {}^t\underline{\underline{\nabla}}\,\underline{u}\right) & \text{for } \underline{x} \in V \\ \underline{\underline{\sigma}} = \underline{\underline{\underline{\underline{C}}}}(\underline{x}) : \underline{\underline{\varepsilon}} & \text{for } \underline{x} \in V \end{cases}, \tag{1}$$

where $\underline{\underline{\underline{\underline{C}}}}(\underline{x})$ is the local stiffness tensor equal to $\underline{\underline{\underline{\underline{0}}}}$ in the air phase and $\underline{\underline{\underline{\underline{C}}}}^{\text{ice}}$ in the ice phase. With the knowledge of the microscopic stress, its homogenized macroscopic counterpart can be computed, and the linear relationship between $\underline{\underline{\Sigma}}$ and $\underline{\underline{\text{E}}}$ gives the homogenized

stiffness tensor $\underline{\underline{\underline{\underline{C}}}}^{\text{hom}}$:

$$\underline{\underline{\Sigma}} = \frac{1}{|V|}\int_V \underline{\underline{\sigma}}\ \mathrm{d}V = \underline{\underline{\underline{\underline{C}}}}^{\text{hom}} : \underline{\underline{\mathrm{E}}}.$$

The homogenized stiffness tensor $\underline{\underline{\underline{\underline{C}}}}^{\text{hom}}$ exhibits only 21 independent components in the most general case. By setting 5 out of 6 of the independent components of $\underline{\underline{\mathrm{E}}}$ equal to 0 ($\underline{\underline{\mathrm{E}}} = \delta_{ij}\,\underline{e}_i \otimes_s \underline{e}_j$ where δ_{ij} is the Kronecker delta), only 6 numerical simulations are needed in order to fully compute $\underline{\underline{\underline{\underline{C}}}}^{\text{hom}}$. However, based on the features of the compliance matrices computed on all the 3D images, it appears reasonable to model snow as an orthotropic material (i.e. a material with two perpendicular planes of symmetry) of principal axes ($\underline{e}_1$,$\underline{e}_2$,$\underline{e}_3$), $\underline{e}_3$ being along the direction of gravity. By doing so, the 21 independent components of $\underline{\underline{\underline{\underline{C}}}}^{\text{hom}}$ are reduced to 9: three Young moduli, three shear moduli and three Poisson ratios (because of the symmetry of the compliance matrix) and the inverse of $\underline{\underline{\underline{\underline{C}}}}^{\text{hom}}$, i.e. the compliance matrix, is written :

$$\begin{pmatrix} \mathrm{E}_{11} \\ \mathrm{E}_{22} \\ \mathrm{E}_{33} \\ 2\mathrm{E}_{23} \\ 2\mathrm{E}_{13} \\ 2\mathrm{E}_{12} \end{pmatrix} = \left(\begin{array}{ccc|ccc} 1/E_1 & -\nu_{12}/E_1 & -\nu_{13}/E_1 & 0 & 0 & 0 \\ -\nu_{21}/E_2 & 1/E_2 & -\nu_{23}/E_2 & 0 & 0 & 0 \\ -\nu_{31}/E_3 & -\nu_{32}/E_3 & 1/E_3 & 0 & 0 & 0 \\ \hline 0 & 0 & 0 & 1/G_{23} & 0 & 0 \\ 0 & 0 & 0 & 0 & 1/G_{13} & 0 \\ 0 & 0 & 0 & 0 & 0 & 1/G_{12} \end{array}\right) \cdot \begin{pmatrix} \Sigma_{11} \\ \Sigma_{22} \\ \Sigma_{33} \\ \Sigma_{23} \\ \Sigma_{13} \\ \Sigma_{12} \end{pmatrix}. \qquad (2)$$

With the use of the Abaqus plugin *HomTools*, the macroscopic homogeneous stress $\underline{\underline{\Sigma}}$ is automatically computed giving thus a straightforward access to the homogenized stiffness tensor (Figure 1).

3. Convergence analysis

Because homogenization theory is based on the assumption of the separation of scales, the fundamental notion of representative elementary volume (REV) is discussed in this section, and the integral range theory [*Lantuejoul*, 1991] is used in order to link REV and

the correlation lengths presented by *Löwe et al.* [2013]. A sensitivity analysis is performed on a given snow sample in order to quantitatively define a dimensionless REV size.

3.1. Dimensionless volume parametrization

According to the integral range theory developed by *Lantuejoul* [1991], *Kanit et al.* [2003] proposed a method for determining the typical REV size of a random heterogeneous material at a given precision. This prediction is based on the fact that the variance $D_Z^2(V)$ of a given physical or mechanical property Z decreases as a power law of the ratio between the sample volume V considered and the integral range A_3 of the material [*Lantuejoul*, 1991]. For a porous material of porosity ϕ, this relation reads:

$$D_Z^2(V) \;=\; \phi(1-\phi)(Z_m - Z_{air})^2 \left(\frac{A_3}{V}\right)^{\alpha_Z} \tag{3}$$

where $Z_m - Z_{air}$ is the property contrast between air and material phases, and α_Z is an exponent smaller than one that depends both on the property and the boundary value problem considered. The bigger the edge effect, the smaller this exponent. It is noteworthy to notice that the integral range A_3 is a geometrical parameter that depends on the microstructure [*Lantuejoul*, 1991; *Kanit et al.*, 2003]. If the two-point correlation function is denoted by

$$C(X, \underline{h}) = p\{\underline{x} \in X, \underline{x} + \underline{h} \in X\},$$

the integral range is defined as

$$A_3 \;=\; \frac{1}{C(X,0) - C(X,0)^2} \int_{R^3} (C(X,\underline{h}) - C(X,0)^2)\, \mathrm{d}\underline{h}. \tag{4}$$

By dividing the sample volume by the integral range of the snow considered, it is possible to restrict the volume convergence analysis of the homogenized mechanical properties

of snow to a single arbitrary snow sample and then define a general size for the REV as a multiple (n) of the integral range for any type of snow thanks to equation (3), i.e $V = n\ A_3$. In practice, the numerical estimate of the integral range appears to be fairly well approximated by the product of the three correlation lengths (ℓ_1, ℓ_2, ℓ_3) along the axes $\underline{e}_1$, $\underline{e}_2$ and $\underline{e}_3$, which can be computed following the approach proposed in *Löwe et al.* [2013].

3.2. Volume convergence analysis

For practical reasons, the volume convergence analysis was not performed in terms of variance but the dimensionless parametrization presented in the previous subsection was used. In order to evaluate the optimal size of the REV of snow, i.e. the optimal value of n, a volume convergence analysis has been performed on a rounded grain (RG) sample of a density of 285 kg.m^{-3} and of a typical correlation length $\ell = \sqrt[3]{\ell_1\ \ell_2\ \ell_3} \simeq \sqrt[3]{A_3}$ of 70 μm. Cubic sub-volumes of size $V = n\ A_3 = (m\ \ell)^3$ were extracted from the raw binary tomographic image and were all meshed with *iso2mesh* with the same meshing options. The homogenized stiffness and compliance matrices were then computed following the approach presented in 2.4. The Figure 1 shows the evolution of the Young moduli with respect to m. A similar plot was also obtained concerning the shear moduli.

This figure highlights the convergence of the young moduli towards a constant value with increasing m. A compromise between a good precision and a reasonable simulation time (approximately 10 hours) has been made and a REV of typical length of 30 ℓ was retained to perform all the simulations. The Figure 1 also shows that the volume convergence is slower for the Young moduli of the sample than for its density. This is to be put in parallel

with the theoretical expression of the variance given in the equation (3) and justifies the approach followed in this paper to not perform the convergence analysis on geometrical properties only.

3.3. Mesh convergence analysis

In parallel, a mesh convergence analysis has been performed on the sub-volume of a typical length scale of $30\,\ell$. The evolution of the Young moduli with respect to the mesh size is given in Figure 1. A very similar plot was also obtained concerning the shear moduli. Again, a compromise between a good precision and a reasonable simulation time has been made and the meshing parameters used for the previous volume convergence analysis were kept.

4. Correlation between density and homogeneous elastic properties

The homogeneous elastic properties of a large variety of snow types were computed following the above methodology on 29 3D images from the database of the snow research center (CEN) (see e.g. [*Calonne et al.*, 2012]). The numerical data used in this study are available in the supplementary material linked to this paper.

4.1. Density influence on the snow elastic properties

Young moduli, shear moduli and Poisson's ratio are plotted with respect to the relative density of snow in Figures 2 and 3. Triple "T" shapes are used to show the relative locations of the Young and shear moduli. While the large and the small bars of the triple "T" correspond to horizontal moduli (respectively E_1 and E_2 or G_{23} and G_{13}), the bottom of the triple "T" corresponds to vertical moduli (E_3 or G_{12}). For the Poison's ratio, the

average value is plotted together with the interval that contains the six Poison's ratio presented in (2). In order to visualize the difference in microstructure of the different samples, color is used in order to highlight the different types of snow according to the international classification [*Fierz et al.*, 2009].

In a log-log scale, the Young and shear moduli dependence with respect to density appears to be relatively linear throughout the wide range tested (from 102 to 544 kg.m^{-3}). A power law fit gives the first order dependence relationships with good regression coefficients (R^2):

$$\begin{cases} \dfrac{E_{\text{snow}}}{E_{\text{ice}}} = 0.78 \left(\dfrac{\rho_{\text{snow}}}{\rho_{\text{ice}}}\right)^{2.33}, \; R^2 = 0.96 \\ \dfrac{G_{\text{snow}}}{G_{\text{ice}}} = 0.96 \left(\dfrac{\rho_{\text{snow}}}{\rho_{\text{ice}}}\right)^{2.55}, \; R^2 = 0.98 \end{cases}, \quad \text{for } \frac{\rho_{\text{snow}}}{\rho_{\text{ice}}} \in [0.1; 0.6]. \tag{5}$$

The numerical points reported in Figure 2 were compared with the prediction of two analytical models and two energy bounds. The Young and shear moduli corresponding to the prediction of the classical Reuss's bound and the Hashin and Shtrikman upper bound for isotropic material [*Hashin and Shtrikman*, 1963] were computed on the range of densities considered. The isotropic differential and Mori-Tanaka schemes, which can still be used for high porosity values, were also simulated. The differential scheme [*Zimmerman*, 1991] consists of an iterative application of the dilute scheme that implies the resolution of an Eshelby problem where the true macroscopic strain is applied on the boundary. The Mori-Tanaka scheme [*Mori and Tanaka*, 1973] consists of an Eshelby problem where an implicit macroscopic strain is applied on the boundary in order to respect the mean strain distribution between matrix and inclusions. Eventually, in order to evaluate the consistency of our implementation of the KUBC homogenization process to snow, the numerical

estimates of the Young modulus in **?** *Srivastava et al.* [2010] and *Schneebeli* [2004] were reported in Figure 2 for comparison.

4.2. Discussion

As visible in Figure 2, the parametrization (5) of the elastic properties of snow by a power law gives reasonable results for the prediction of the Young and shear moduli of snow on the whole range of densities explored. It is interesting here to draw a parallel with the analytical models classically used for the elastic properties of cellular materials [*Knackstedt et al.*, 2006; *Gibson and Ashby*, 1999]. Indeed, for skeleton cellular materials locally loaded in bending, the relative Young modulus of the porous material is given by a power law of exponent $n = 2$ of its relative density. However for membrane cellular materials locally loaded in bending, the relative Young modulus is given by a power law of exponent $n = 3$ of its relative density. The exponent of the fitted law (5) is consistent with the predicted behavior of these materials also characterized by a very high porosity. Under the hypothesis that the ice grains are loaded in bending too, the macroscopic behavior of snow is closer to a skeleton behavior than a membrane one.

Concerning the comparison with the differential and Mori-Tanaka schemes in Figure 2, the differential scheme is found to overestimate the values of the Young modulus but gives a relatively good prediction of the exponent of the power law linking relative Young modulus and relative density. For the shear modulus, the differential scheme is not satisfactory anymore. As for Poisson's ratio in Figure 3 the Mori-Tanaka scheme proves to give a relatively good estimate contrary to the differential scheme. The two analytical

schemes considered were initially developed in order to model inclusion/matrix materials and it is not surprising that they cannot account for the connected porosity of snow.

The results of *Srivastava et al.* [2010] in Figure 2 computed on a limited range of densities appear to be of the same order of magnitude as the results presented in this paper. The results obtained by **?** on a wide range of densities are not consistent with our results. The exponential fit proposed by **?** is plotted on Figure 2 and a power law with a good regression coefficient of $R^2 = 0.917$ has been proposed to better fit the data :

$$\frac{E_{\text{snow}}}{E_{\text{ice}}} = 5.73 \left(\frac{\rho_{\text{snow}}}{\rho_{\text{ice}}} \right)^{5.15}.$$

The major difference between our approach and those found in the literature lies in the boundary value problem used in the homogenization procedure. While we use KUBC boundary conditions, **?** uses a uniaxial compression test that requires a much bigger size of VER. In order to deduced the Young modulus value from numerical simulations, **?** were forced to postulate a macroscopic isotropic behavior for all their samples. Further more, the resolution of the images used by **?** is only a tenth of the resolution used to design our finite element meshes. These differences in the testing procedure might result in the observed differences in Figure 2.

The last comment to be made on the results shown in Figures 2 and 3 is that many samples present an anisotropic behavior that cannot be captured by the density parametrizations of the macroscopic properties of snow given in (5). The degree of anisotropy of a given type of snow can be reckoned thanks to the definition of two indicators $A(E)$ and $A(G)$ such that :

$$A(E) = \frac{E_3}{(E_1 + E_2)/2}, \qquad A(G) = \frac{G_{12}}{(G_{23} + G_{13})/2}, \tag{6}$$

where E_3 and G_{12} are the Young and shear moduli linked to the vertical direction. For all the samples considered, we have $A(E) \in [0.56; 1.57]$ and $A(G) \in [0.77; 1.47]$ while a perfectly isotropic material would exhibit anisotropy indicators equal to 1.

5. Influence of the type of metamorphism on the mechanical properties

As already shown by *Srivastava et al.* [2010] and *Schneebeli* [2004] for mechanical properties or by *Calonne et al.* [2014] for thermal conductivity for instance, the metamorphism of snow, even when occurring at constant density strongly influences its macroscopic behavior. The full 3D homogenization approach implemented here enables the quantitative analysis of these anisotropic mechanical properties. In this section, three types of snow metamorphism are considered in order to reckon their influence on the mechanical properties of snow.

5.1. Temporal evolutions of snow microstructures

In Figure 4 the time evolution of the three Young moduli and the three shear moduli are plotted for each of the three temporal evolutions considered: a temperature gradient experiment, a wet snow metamorphism experiment and an isothermal experiment. In this Figure the subscript 3 corresponds to the vertical direction. In order to reckon the influence of variations in density with time, its time evolution is also plotted in Figure 4.

Temperature gradient experiment: The first temporal series considered consists of the seven micro-tomographic images of *Calonne et al.* [2014]. They were obtained during a temperature gradient experiment at -4 $^\circ$C. A temperature gradient of 43 K.m^{-1} was applied to a sieved snow layer during 500 h and samples were regularly extracted

from the middle of the layer, impregnated with 1-chloronaphtalene and stored at -20 $^\circ$C. They were then imaged by microtomography.

On the corresponding plot of Figure 4, it can be seen that the general fluctuations of the relative moduli follow the small fluctuations in density observed between the different images. In addition to that, the development of an anisotropic mechanical behavior can be seen with the apparition of an increasing gap between the vertical Young modulus E_3 and the two other ones, and between the horizontal shear modulus G_{12} and the two other ones.

Wet snow metamorphism experiment: The second temporal series considered consists of 5 micro-tomographic images taken from *Flin et al.* [2011]. They were obtained during a grain coarsening experiment. Snow porosity was saturated with water kept at 0 $^\circ$C and the coarsening of this wet snow was monitored over 142 h by sampling several specimens and imaging them by X-ray microtomography.

After a fast evolving phase at the begining of the experiment, the Young and shear moduli evolve in an isotropic way.

Isothermal experiment: The third temporal series considered consists of the first 8 micro-tomographic images of *Flin et al.* [2004]. 15 h after a snowfall, a natural snow layer was kept under isothermal conditions and the metamorphism of the snow microstructure was monitored over 3 months by sampling several specimens and imaging them by X-ray microtomography.

On the corresponding plot of Figure 4, the time evolution of both the Young and shear moduli follows the increasing density.

5.2. Discussion

Temperature gradient experiment: In Figure 4, the fast initial decrease in the values of the Young moduli might be related to the initial sublimation of the small ice bridges between ice grains [*Calonne et al.*, 2014]. Because of the vertical orientation of the vapor fluxes, horizontal bridges are more likely to be broken than the vertical ones. This is to be linked with the lower initial decrease of the vertical Young modulus E_3. With the lengthening of the ice crystals in the vertical direction combined with vertical air chimneys due to sublimation/deposition phenomena, more ice is involved in vertical compression or shear solicitations than in their horizontal counterparts. This microstructure evolution is thus consistent with the relative increase in the vertical Young modulus E_3 and the vertical shear moduli G_{13} and G_{23} and with the results of *Calonne et al.* [2014] concerning the physical and geometrical properties of snow (thermal conductivity, Gaussian curvature, ...). During the experiment, the anisotropy indicators $A(E)$ and $A(G)$ defined in (6) vary from respectively 0.89 and 1.08 at the begining of the experiment to 1.56 and 0.83 in the end. Overall, most of the moduli decrease from the initial to the final state, which is consistent with the well-known fact that temperature gradient metamorphism is a cause of weak snow layer formation.

These observations can be compared to the results obtained by *Srivastava et al.* [2010] for a similar temperature gradient experiment. Their findings are consistent with ours except the fact that they observed an increase in density at the beginning of their experiment. This explains why they didn't observe any initial decrease of the Young and shear moduli.

Wet snow metamorphism experiment: In Figure 4, the first increase in density is to be related to residual liquid water that remained in the sample due to capillary forces and froze before the sample was completely dried. Then the Young and shear moduli remain constant and evolve in a very isotropic way ($A(E) \in [1.00; 1.12]$ and $A(G) \in [0.94; 1.00]$). The observed stagnation can be quite puzzling because the microstructure is modified in a noticeable way during this experiment. However this can be explained by the fact that the ice bridges between ice grains are growing and, in the meantime, their number per volume unit is decreasing. Overall, such a metamorphism seems to have little impact on the snow mechanical properties as far as the liquid water has been drained before refreezing. Otherwise, the increase in density due to refreezing would significantly strengthen the structure which is consistent with the practical knowledge of melt freeze effect on the mechanical properties of snow.

Isothermal experiment: In Figure 4, the densification of snow is quantified with the increase in density due to the creeping of snow under its own weight. Because of the relatively small thickness of the snow layer considered (about 10 cm), no huge anisotropy appears with respect to the privileged vertical direction of compaction. During all the experiment, the anisotropy indicators remain relatively constant with $A(E) \in [0.85; 1.03]$ and $A(G) \in [0.95; 1.28]$. However, as it has been observed by *Flin et al.* [2004], the snow grains tend to rearrange with their longest dimension along the horizontal direction. This might be related to the fact that the vertical Young modulus is systematically the lowest one after 600 h. Overall, such a metamorphism results in a noticeable densification of snow, and thus in an increase of its stiffness. Recent snow on top of the snowpack evolves

in a relatively isotropic way under isothermal creeping. This observation is consistent with the practical knowledge that the mechanical stability of the snowpack is increasing with time after a snowfall, providing that no temperature gradient metamorphism is at stake.

6. Conclusion and Outlooks

In this work, a numerical homogenization method that can capture the full 3D macroscopic mechanical behavior of snow was successfully developed. A rigorous use of the theoretical results of the homogenization theory was made in the definition of the boundary value problem to be solved. Contrary to most of the previous studies on the subject, the convergence analysis was performed in a dimensionless form and in terms of physical and not geometrical parameters.

Thanks to this powerful numerical procedure, a much wider range of density and a greater diversity of microstructures has been explored in this paper than in previous studies. Over the whole range of density tested, simple power laws have been proposed in order to link the Young and shear moduli of snow to its density.

Thanks to the study of three temporal series, the influence of the three main types of metamorphism on the macroscopic elastic properties was successfully reckoned. The numerical results obtained are in good agreement with the qualitative effects each metamorphism type has on the mechanical properties of snow.

In the future, the proposed methodology might be easily transposed to the study of other materials, provided that the 3D images of their microstructure is available and that the constitutive behavior of their constituents is known. Our numerical procedure can

easily be applied to investigate a more complex behavior of snow such as its 3D viscoplastic behavior. Such a work is currently in progress.

Acknowledgments. We thank S. Lejeunes and S. Bourgeois from the LMA for sharing with us the code of their plugin HOMTOOLS and for helping us to use it in our scripts. We thank PK. Srivastava for accepting to share with us the numerical data of *Srivastava et al.* [2010]. CNRM-GAME/CEN is part of the LabEx OSUG@2020 (ANR10 LABX56). 3SR lab is part of the LabEx Tec 21 (Investissements d'Avenir - grant agreement ANR11 LABX0030).

References

Auriault, J.-L., C. Boutin, and C. Geindreau (2010), *Homogenization of coupled phenomena in heterogenous media*, vol. 149, John Wiley & Sons.

Brzoska, J.-B., C. Coléou, B. Lesaffre, S. Borel, O. Brissaud, W. Ludwig, E. Boller, and J. Baruchel (1999), 3D visualization of snow samples by microtomography at low temperature, *ESRF Newsletter*, *32*, 22–23.

Calonne, N., F. Flin, S. Morin, B. Lesaffre, S. R. du Roscoat, and C. Geindreau (2011), Numerical and experimental investigations of the effective thermal conductivity of snow, *Geophys. Res. Lett.*, *38*, L23,501, doi:10.1029/2011GL049234.

Calonne, N., C. Geindreau, F. Flin, S. Morin, B. Lesaffre, S. Rolland du Roscoat, and P. Charrier (2012), 3-d image-based numerical computations of snow permeability: links to specific surface area, density, and microstructural anisotropy, *The Cryosphere*, *6*(5), 939–951, doi:10.5194/tc-6-939-2012.

Calonne, N., F. Flin, C. Geindreau, B. Lesaffre, and S. Rolland du Roscoat (2014), Study of a temperature gradient metamorphism of snow from 3-d images: time evolution of microstructures, physical properties and their associated anisotropy, *The Cryosphere Discussions*, *8*, 1407–1451.

Chandel, C., P. K. Srivastava, and P. Mahajan (2014), Micromechanical analysis of deformation of snow using x-ray tomography, *Cold Regions Science and Technology*, *101*, 14–23.

Dormieux, L., and E. Bourgeois (2002), *Introduction à la micromécanique des milieux poreux*, Presses de l'École nationale des ponts et chaussées.

Fang, Q., and D. A. Boas (2009), Tetrahedral mesh generation from volumetric binary and grayscale images, in *Biomedical Imaging: From Nano to Macro, 2009. ISBI'09. IEEE International Symposium on*, pp. 1142–1145, IEEE.

Fierz, C., R. L. Armstrong, Y. Durand, P. Etchevers, E. Greene, D. M. McClung, K. Nishimura, P. K. Satyawali, and S. A. Sokratov (2009), *TheInternational Classificationi for Seasonal Snow on the Groun*, UNESCO/IHP.

Flin, F., and J.-B. Brzoska (2008), The temperature-gradient metamorphism of snow: vapour diffusion model and application to tomographic images, *Annals of Glaciology*, *49*(1), 17–21.

Flin, F., J.-B. Brzoska, B. Lesaffre, C. Coléou, and R. A. Pieritz (2004), Three-dimensional geometric measurements of snow microstructural evolution under isothermal conditions, *Annals of glaciology*, *38*(1), 39–44.

Flin, F., B. Lesaffre, A. Dufour, L. Gillibert, A. Hasan, S. Rolland du Roscoat, S. Cabanes, and P. Pugliese (2011), On the computations of specific surface area and specific grain contact area from snow 3d images, *Physics and Chemistry of Ice*, pp. 321–328.

Gibson, L. J., and M. F. Ashby (1999), *Cellular solids: structure and properties*, Cambridge university press.

Hagenmuller, P., T. C. Theile, and M. Schneebeli (2014), Numerical simulation of microstructural damage and tensile strength of snow, *Geophys. Res. Lett.*, *41*(1), 86–89, doi:10.1002/2013GL058078.

Hashin, Z., and S. Shtrikman (1963), A variational approach to the theory of the elastic behaviour of multiphase materials, *Journal of the Mechanics and Physics of Solids*, *11*(2), 127–140.

Kaempfer, T. U., M. Schneebeli, and S. Sokratov (2005), A microstructural approach to model heat transfer in snow, *Geophysical Research Letters*, *32*(21).

Kanit, T., S. Forest, I. Galliet, V. Mounoury, and D. Jeulin (2003), Determination of the size of the representative volume element for random composites: statistical and numerical approach, *International Journal of solids and structures*, *40*(13), 3647–3679.

Knackstedt, M. A., C. H. Arns, M. Saadatfar, T. J. Senden, A. Limaye, A. Sakellariou, A. P. Sheppard, R. M. Sok, W. Schrof, and H. Steininger (2006), Elastic and transport properties of cellular solids derived from three-dimensional tomographic images, *Proceedings of the Royal Society A: Mathematical, Physical and Engineering Science*, *462*(2073), 2833–2862.

Lantuejoul, C. (1991), Ergodicity and integral range, *Journal of Microscopy*, *161*(3), 387–403.

Lejeunes, S., S. Bourgeois, et al. (2011), Une toolbox abaqus pour le calcul de propriétés effectives de milieux hétérogènes, in *10e colloque national en calcul des structures*.

Löwe, H., F. Riche, and M. Schneebeli (2013), A general treatment of snow microstructure exemplified by an improved relation for thermal conductivity, *The Cryosphere*, *7*(5), 1473–1480, doi:10.5194/tc-7-1473-2013.

Mellor, M. (1974), *A review of basic snow mechanics*, US Army Cold Regions Research and Engineering Laboratory.

Mori, T., and K. Tanaka (1973), Average stress in matrix and average elastic energy of materials with misfitting inclusions, *Acta metallurgica*, *21*(5), 571–574.

Pieritz, R. A., J.-B. Brzoska, F. Flin, B. Lesaffre, and C. Coléou (2004), From snow x-ray microtomograph raw volume data to micromechanics modeling: first results, *Ann. Glaciol.*, *38*, 52–58, (10.3189/172756404781815176).

Pinzer, B., M. Schneebeli, and T. Kaempfer (2012), Vapor flux and recrystallization during dry snow metamorphism under a steady temperature gradient as observed by time-lapse micro-tomography, *The Cryosphere Discussions*, *6*(3), 1673–1714.

Riche, F., M. Montagnat, and M. Schneebeli (2013), Evolution of crystal orientation in snow during temperature gradient metamorphism, *Journal of Glaciology*, *59*(213), 47–55.

Schleef, S., H. Löwe, and M. Schneebeli (2014), Hot-pressure sintering of low-density snow analyzed by x-ray microtomography and in situ microcompression, *Acta Materialia*, *71*,

185–194.

Schneebeli, M. (2004), Numerical simulation of elastic stress in the microstructure of snow, *Annals of Glaciology*, *38*(1), 339–342.

Schulson, E. M., P. Duval, et al. (2009), *Creep and fracture of ice*, Cambridge University Press Cambridge.

Shapiro, L. H., J. B. Johnson, M. Sturm, and G. L. Blaisdell (1997), Snow mechanics: review of the state of knowledge and applications.

Srivastava, P., P. Mahajan, P. Satyawali, and V. Kumar (2010), Observation of temperature gradient metamorphism in snow by x-ray computed microtomography: measurement of microstructure parameters and simulation of linear elastic properties, *Annals of Glaciology*, *51*(54), 73–82.

Van Rietbergen, B., A. Odgaard, J. Kabel, and R. Huiskes (1996), Direct mechanics assessment of elastic symmetries and properties of trabecular bone architecture, *Journal of Biomechanics*, *29*(12), 1653–1657.

Zimmerman, R. W. (1991), Elastic moduli of a solid containing spherical inclusions, *Mechanics of Materials*, *12*(1), 17–24.

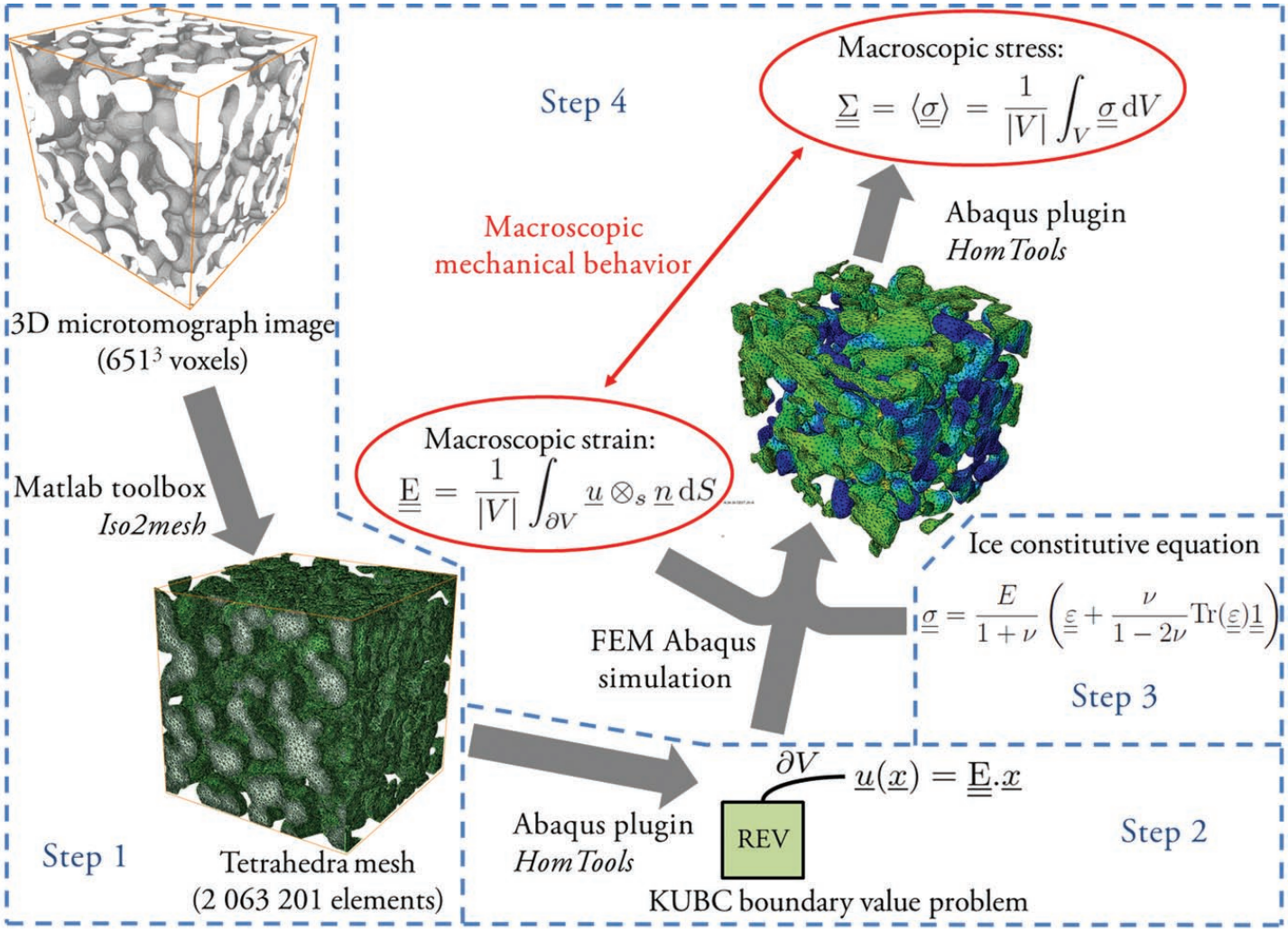

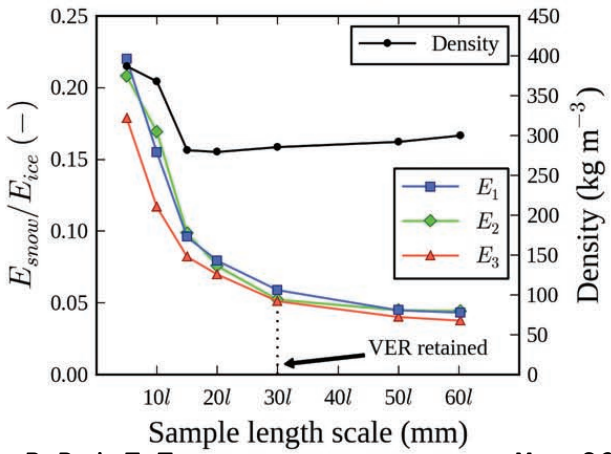

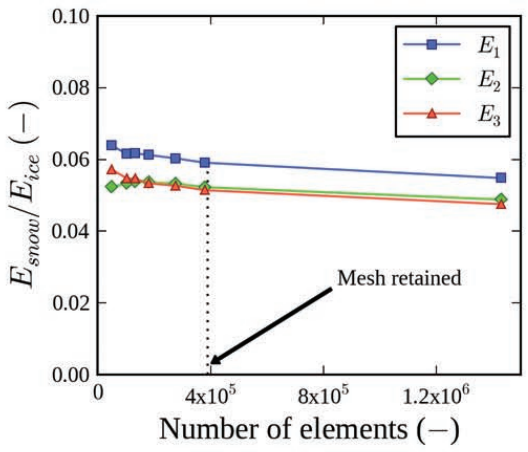

Figure 1. Four steps procedure used in order to transform 3D microtomograph images of snow into finite element models and numerically solve KUBC homogenization boundary value problems (top). Young modulus convergence analysis with respect to the dimentionless size of the sample and the size of the mesh used (bottom). Concerning the volume

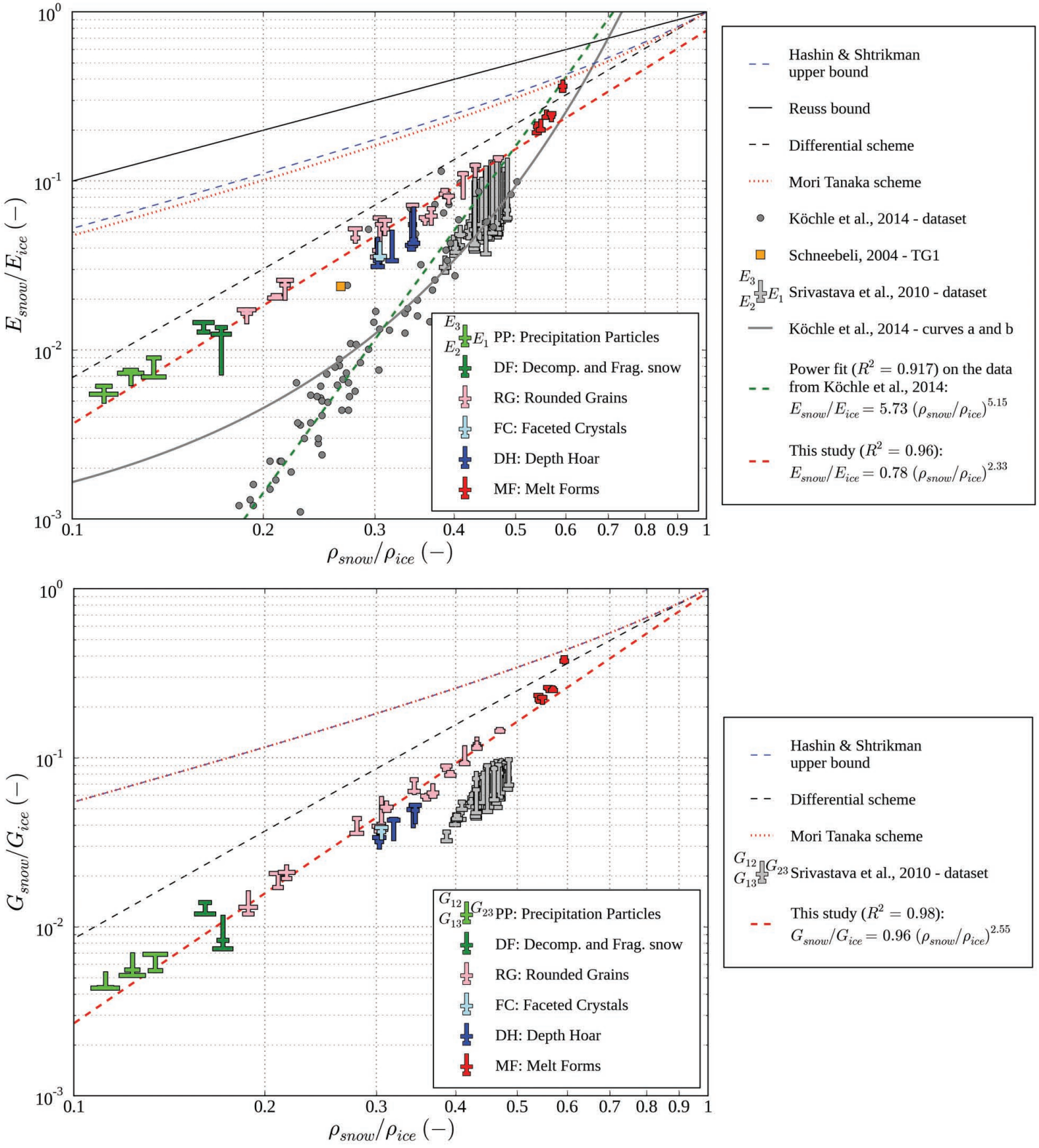

Figure 2. Young moduli (top) and shear moduli (bottom) dependence with respect to density. Triple "T" shapes are used in order to distinguish the moduli. Color is used in order to highlight the different snow types according to the international classification [*Fierz et al.*, 2009]. The points found in **?**, *Srivastava et al.* [2010] and *Schneebeli* [2004] are reported, and comparison is made with two energy bounds and two analytical estimates.

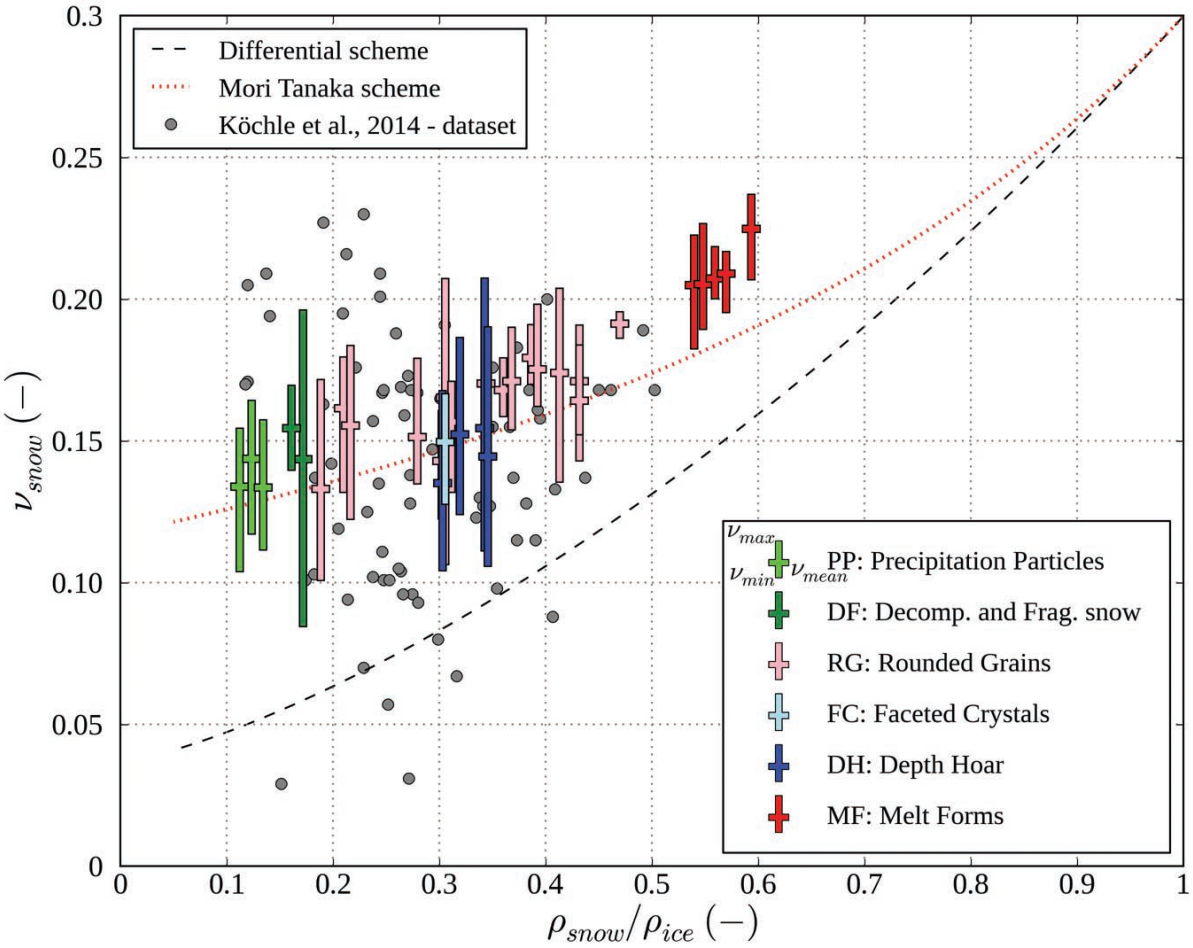

Figure 3. Average Poison's ratio dependence with respect to density. Vertical bars show the location of the highest and lowest Poison's ratio. Color is used in order to highlight the different snow types according to the international classification [*Fierz et al.*, 2009]. Comparison is made with two analytical estimates and the data from **?**.

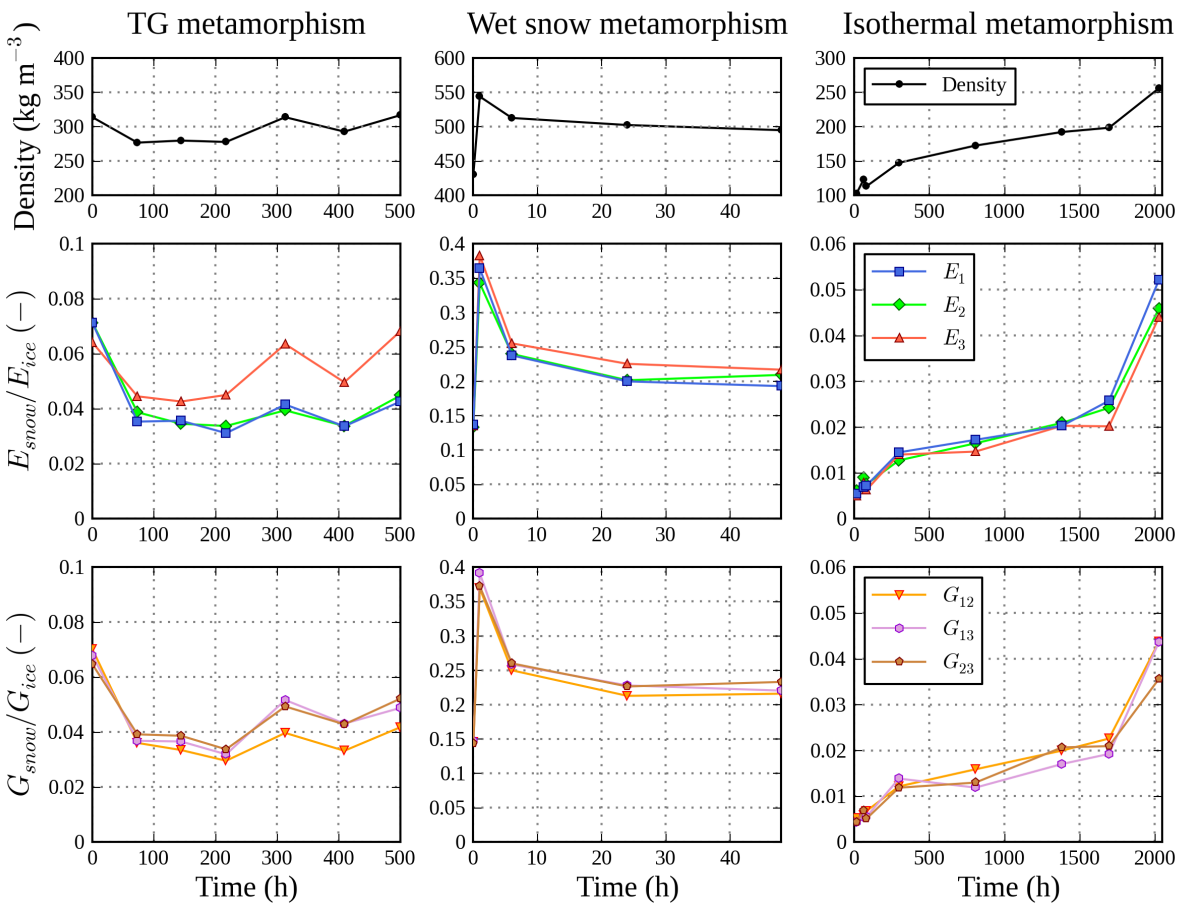

Figure 4. Time evolution of the three Young moduli (middle) and the three shear moduli (bottom) of snow during three temporal experiments. The index 3 corresponds to the direction of gravity. The time evolution of the snow density is also represented (top).